ACS APPLIED NANO MATERIALS

www.acsanm.org Article

# Hybridization of the A- and B-Exciton in a $WS_2$ Monolayer Mediated by the Transverse Electric Polarized Wave Supported by a $Si_3N_4$/Ag Heterostructure

Weichen He, Shimei Liu, Jingting Liu, Shulei Li, Fu Deng, Haiying Liu, Haihua Fan, Jun Dai, and Sheng Lan*

Cite This: https://doi.org/10.1021/acsanm.4c02981 Read Online

ACCESS | Metrics & More | Article Recommendations | Supporting Information

**ABSTRACT:** Realizing and manipulating strong light−matter coupling in two-dimensional monolayer semiconductors is important in the research of cavity quantum electrodynamics and the development of photonic/plasmonic devices. Here, we investigate the coupling between the transverse-electric (TE) polarized wave supported by a $Si_3N_4$/Ag heterostructure and the two excitons in a $WS_2$ monolayer (i.e., the A- and B-excitons) attached on such a heterostructure. It is found that the dissipation rate of the TE wave can be modified by simply varying the thickness of the Ag film. By appropriately designing the thickness of the Ag film, the strong coupling between the TE wave and the two excitons in the $WS_2$ monolayer can be simultaneously realized, leading to hybridization of the two excitons. We numerically simulate the angle-resolved reflection spectra for the $WS_2/Si_3N_4$/Ag heterostructure and reveal hybridization of the two excitons mediated by the TE wave. In experiments, we introduce Au nanorods as scatters for the TE wave, which enhance the in-plane electric field and achieve stronger photon−exciton coupling. We experimentally measured the angled-resolved scattering spectra for an Au nanorod placed on the $WS_2/Si_3N_4$/Ag heterostructure and demonstrated the strong coupling between the TE wave and the two excitons, which results in the hybridization of the two excitons. Our findings open horizons for realizing and manipulating strong light−matter interaction in two-dimensional materials and pave the way for the construction of photonic/plasmonic devices by exploiting dielectric−metal heterostructure.

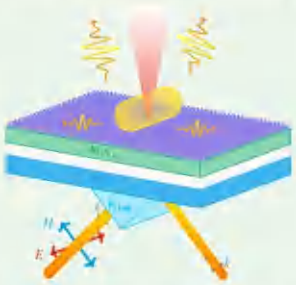

**KEYWORDS:** *$WS_2$ monolayer, $Si_3N_4$/Ag heterostructure, strong coupling, hybridization, Au nanorod, dark-field scattering*

## 1. INTRODUCTION

Light−matter interaction has long been the focus of scientific research since the invention of the first laser. In recent years, strong coupling between photons/plasmons and excitons has attracted great interest due to its potential applications in quantum manipulation, ultrafast switching, and low threshold laser, etc.[1−3] When the rate of coherent energy transfer between photons/plasmons and excitons exceeds their average dissipation rate, the system enters into the strong coupling regime, resulting in the formation of part-light and part-matter quasi-particles called polaritons.[4,5]

An exciton placed in an optical microcavity can interact with the photon mode of the microcavity, and the strong coupling between them leads to the formation of the so-called microcavity polariton. When multiple excitonic resonances are coupled using a single cavity mode, the excitons are said to be hybridized or mixed. Such a hybridization has been successfully realized for both Frenkel and Wannier−Mott excitons.[6,7] Hybridization of Frenkel and Wannier−Mott excitons has also been demonstrated in an organic−inorganic hybrid optical microcavity via strong exciton−photon coupling and photon mediation.[8,9] Hybrid exciton−photon structures represent promising model systems for exploring energy capture, storage, and transfer among coherently coupled molecular excitations. Therefore, an investigation of hybrid cavity polaritons can improve our understanding of how energy transfer occurs between semiconductors with different properties.

In 2014, it was demonstrated that the hybrid-polariton states formed in an optical microcavity by mixing the electronic transitions of two J-aggregated molecular dyes can act as an efficient and ultrafast energy-transfer pathway between the two exciton states.[10] In 2017, the hybridization of two fluorescent dyes within a microcavity was achieved by coupling different exciton transitions to the same cavity mode. The relative population of different polariton branches following non-resonant laser excitation can be manipulated by changing cavity detuning.[11] In addition, the nonradiative energy transfer between spatially separated molecules becomes feasible when

Received: May 22, 2024
Revised: July 25, 2024
Accepted: July 26, 2024







https://doi.org/10.1021/acsanm.4c02981
ACS Appl. Nano Mater. XXXX, XXX, XXX−XXX

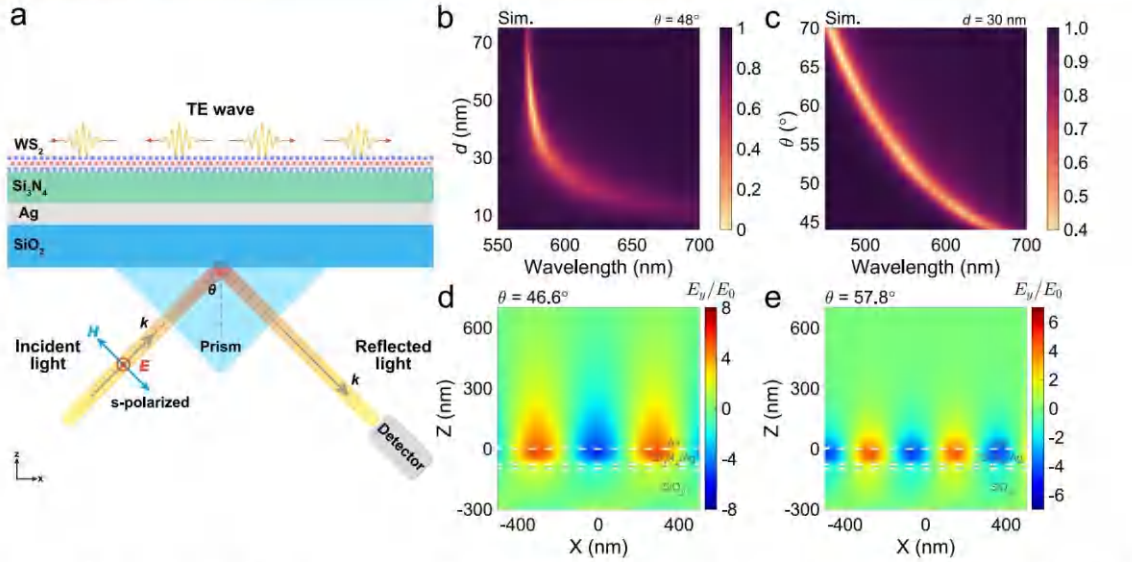


**Figure 1.** (a) Schematic showing the excitation of TE wave on a $WS_2/Si_3N_4/Ag$ heterostructure by using prism coupling. (b) Two-dimensional reflection spectra calculated for $Si_3N_4/Ag$ heterostructures composed of Ag films with different thicknesses. The incident angle is chosen to be $\theta = 48°$. (c) Two-dimensional reflection spectra calculated for a $Si_3N_4/Ag$ heterostructure ($d = 30$ nm) at different incident angles. The in-plane electric field ($E_y/E_0$) distributions at the resonant wavelengths of the A- and B-exciton for the $Si_3N_4/Ag$ heterostructure with $d = 30$ nm are shown in (d) and (e), respectively. In each case, the incident angle is also provided.

the excitonic state of each molecule is strongly coupled to the same optical microcavity mode. If the coupling strength remains unchanged, the energy transfer process becomes independent of distance.[12,13] One specific application of this hybridization is the enhanced energy transfer between the donor and the acceptor when they are strongly coupled. The energy is transferred via the middle polariton, which combines the contributions of both the donor and acceptor.

So far, strong photon−exciton and plasmon−exciton coupling have been demonstrated in various systems composed of J-aggregates,[14−17] dye molecules,[18] and quantum dots.[19−21] However, the coupling strength between photons and excitons is limited by the small transition dipole moments of the excitons in these materials (4−36 D).[14,18,21,22] In recent years, transition metal dichalcogenides (TMDCs) have attracted much attention due to their exotic electronic and optical responses. Monolayer TMDCs are usually semiconductors with direct bandgaps, in which excitons possess large binding energies (0.3−0.9 eV)[23] and transition dipole moments (56 D).[24] In addition, monocrystalline TMDCs exhibit uniform optical properties across the entire two-dimensional flake and guarantee the robustness of the strong coupling effect.[25] Due to these excellent properties, monolayer TMDCs are considered as promising candidates for realizing strong coupling.

Using TMDCs as excitonic materials, strong plasmon−exciton coupling or photon−exciton coupling has been successfully demonstrated in a variety of plasmonic and photonic cavities, including individual plasmonic nanoparticles (such as Au nanorods,[25,26] Ag nanorods,[27] and Ag nanoprisms[28−30]), nanoparticle on mirror systems (such as Si nanospheres on mirror,[31,32] Au nanospheres on mirror,[33] and Ag nanocubes on mirror[34−37]), plasmonic arrays (such as Ag nanodisk array[38−42]), high-index dielectric nanoparticles (such as Si nanospheres[43]), and core−shell structures.[44]

Apart from three-dimensional micro- and nanocavities, strong photon/plasmon−exciton coupling can also be realized by using two-dimensional micro- and nanocavities. In these cases, the photon−plasmon energy can be easily modified by changing the angle of the incident light. For example, Liu et al. embedded a $MoS_2$ monolayer into a $Si_3N_4/SiO_2$ distributed Bragg reflector and adjusted the energy detuning by changing the angle of the incident light.[45] Deng et al. used the Kretschmann−Raether configuration to generate surface plasmon polaritons (SPPs) on the surface of a thin Au film and shifted the SPPs by simply changing the incident angle.[46] Recently, Li et al. proposed a $Si_3N_4/Ag$ heterostructure supporting both transverse-electric (TE) and transverse-magnetic (TM) polarized surface waves.[47] The resonant wavelength of the TE wave is highly sensitive to the incident angle, the thickness of the dielectric layer, and the refractive index of the environment. The spatial separation of the electric and magnetic fields is responsible for the large quality factor or the narrow line width of the TE wave. As compared with the TM wave (or the SPPs), the TE wave possesses a larger enhancement factor for the in-plane electric field, implying a stronger interaction with the two-dimensional material attached on the heterostructure.

Basically, the coupling strength between photons/plasmons and excitons in a cavity−TMDC system is determined by the electric field enhancement provided by the cavity and the transition dipole moment of the exciton in the TMDC. For commonly used TMDCs, such as $WS_2$ and $MoS_2$, they usually have more than one exciton resonance. So far, most studies focus on the A-exciton ($X_A$) which possesses a much larger optical absorption and dipole moment, and less attention has been paid to the B-exciton ($X_B$). However, the existence of two


https://doi.org/10.1021/acsanm.4c02981
ACS Appl. Nano Mater. XXXX, XXX, XXX−XXX

excitons offers us the opportunity to realize the exciton hybridization in such a TMDC (e.g., in a $WS_2$ monolayer) through the simultaneous coupling of the two excitons with a photonic or plasmonic mode. It implies that the energy exchange between the A- and B-exciton may become possible if a strong coupling between a photonic/plasmonic mode and the two excitons can be achieved. Recently, Rose et al. investigated the coupling between the SPPs generated on a thin Ag film and the excitons in a few-layer $MoS_2$ and observed the hybridization of the A- and B-exciton.[48] Unfortunately, the coupling strength between the SPPs and the excitons in few-layer $MoS_2$ does not satisfy the strong coupling criterion due to the large dissipation rate of the SPPs. Recently, we successfully demonstrated the strong coupling between the TE wave propagating on a $Si_3N_4$/Ag heterostructure and the two excitons (A- and B-exciton) in a $WS_2$ monolayer.[49] However, hybridization of the A- and B-exciton was not observed.

In this article, we demonstrated numerically and experimentally the hybridization of the A- and B-exciton in a $WS_2$ monolayer mediated by the TE wave supported by a $Si_3N_4$/Ag heterostructure. It was found that the dissipation rate of the TE wave can be modified by simply varying the thickness of the Ag film. The hybridization of the A- and B-exciton can be realized by deliberately adjusting the dissipation rate of the TE wave. In experiments, we introduced gold (Au) nanorods as scatterers for the TE wave to characterize the coupling between the TE wave and the two excitons in the $WS_2$ monolayer. It was confirmed by the angle-resolved scattering spectra of the Au nanorod that the coupling between the TE wave and the two excitons enters into the strong coupling regime. It was revealed that the contribution of the A- or B-exciton to the middle polariton branch exceeds 12%, verifying undoubtedly the hybridization of the two excitons.

## 2. RESULTS AND DISCUSSION

**2.1. Hybridization of the A- and B-Exciton in a $WS_2$ Monolayer Mediated by the TE Wave.** In Figure 1a, we show schematically the TE wave propagating on a dielectric−metal heterostructure composed of a $Si_3N_4$ layer and an Ag film, which are deposited sequentially on a $SiO_2$ substrate. It is excited using s-polarized light in the Kretschmann−Raether configuration.

In a previous study, we found that the resonant wavelength of the TE wave can be modified by changing the incident angle or thickness of the $Si_3N_4$ layer. However, the influence of the thickness of the Ag film on the TE wave was not examined.[47] We investigated a $Si_3N_4$/Ag heterostructure composed of a 100 nm thick $Si_3N_4$ layer and a 50 nm thick Ag film. In this case, the line widths (full width at the half-maximum or FWHM) of the TE wave were found to be ∼36 and ∼56 meV at the resonant wavelengths of the A- and B-exciton, respectively. Although strong photon−exciton coupling was realized for both the A- and B-exciton, the hybridization of the two excitons was not achieved due to the narrow line width (or small dissipation rate) of the TE wave.[49] Physically, a TE wave with a dissipation rate comparable to those of the exciton resonances is beneficial for realizing the strong coupling between the TE wave and the two exciton resonances. On the other hand, however, a TE wave with a large dissipation rate (or broad line width) will facilitate the hybridization of the two excitons. Therefore, there should be an optimum dissipation rate for the TE wave to realize exciton hybridization in a $WS_2$ monolayer through the strong coupling between the TE wave and the two excitons.

In Figure 1b we present the 2D reflection spectra calculated for $Si_3N_4$/Ag heterostructures composed of Ag films with different thicknesses. The incident angle is chosen to be $\theta$ = 48°. As the thickness of the Ag film decreases, one can see a red-shift of the resonant wavelength, a broadening of the line width, and a reduction of the reflectivity (see the Supporting Information, Section S3). This behavior implies that the dissipation rate of the TE wave, which is crucial in coupling with the exciton, can be modified by varying the thickness of the Ag film. By choosing an appropriate thickness for the Ag film, it is possible to realize the hybridization of the A- and B-exciton in the $WS_2$ monolayer. We also calculated the line widths of the TE wave supported by $Si_3N_4$/Ag heterostructures composed of Ag films with different thicknesses at the wavelength corresponding to $\omega_0 \approx \frac{1}{2}(\omega_A + \omega_B)$ (∼561 nm) (see Figure S4). It was observed that the line width of the TE wave is increased from 22.63 to 74.58 meV when the thickness of the Ag film is reduced from 50 to 30 nm (see Figure S5). This line width (74.58 meV) is larger than that of the A-exciton (∼33 meV) and comparable to that of the B-exciton (∼80 meV). In this case, the criterion for strong photon−exciton coupling is still satisfied for the B-exciton. A further reduction of the thickness to $d$ = 20 nm leads to a much broader line width for the TE wave, and the strong coupling criterion is not fulfilled. Therefore, we think that the optimum thickness of the Ag film for realizing the exciton hybridization is $d$ = 30 nm.

In this work, we consider $Si_3N_4$/Ag heterostructures in which the thickness of the $Si_3N_4$ layer is fixed at 75 nm and the thickness of the Ag film ($d$) is variant (see the Supporting Information, Section S4). In Figure 1c, we show the reflection spectra calculated for the $Si_3N_4$/Ag heterostructure with $d$ = 30 nm at different incident angles. The dissipation rates of the TE wave at the resonant wavelengths of the A- and B-exciton are found to be ∼99 and ∼115 nm, respectively. Apparently, these values are much larger than those observed in the $Si_3N_4$/Ag heterostructure with a 100 nm thick $Si_3N_4$ layer and a 50 nm thick Ag film. In Figures 1d and 1e, we present the in-plane electric field ($E_y/E_0$) distribution in the $Si_3N_4$/Ag heterostructure with $d$ = 30 nm at the two exciton resonances. In this case, the electric field contains only the $y$-component, and the enhancement factor is defined as $E_y/E_0$, where $E_0$ is the amplitude of the incident light. As shown in Figure 1b, the dissipation rate of the TE wave is increased with decreasing thickness of the Ag film. When the thickness of the Ag film is reduced from 50 to 30 nm, the enhancement factor for the in-plane electric field at the wavelength of the A-exciton is reduced from ∼8.01 to ∼5.22. Similarly, the enhancement factor for the in-plane electric field at the wavelength of the B-exciton is reduced from ∼6.99 to ∼4.41 (see the Supporting Information, Sections S5 and S6).

In Figure 2a, we show the reflection spectra of the $WS_2$/$Si_3N_4$/Ag heterostructure ($d$ = 30 nm) excited using s-polarized light at different incident angles. One can observe the splitting of the exciton resonance at $\theta$ = 49° and $\theta$ = 61°, where the energy of the TE wave coincides with the energies of the A- and B-exciton, respectively. In Figure 2b, we present the 2D reflection spectra of the $WS_2$/$Si_3N_4$/Ag heterostructure. One can clearly identify anticrossing behaviors around the two exciton resonances of the $WS_2$ monolayer, indicating the



https://doi.org/10.1021/acsanm.4c02981
ACS Appl. Nano Mater. XXXX, XXX, XXX−XXX

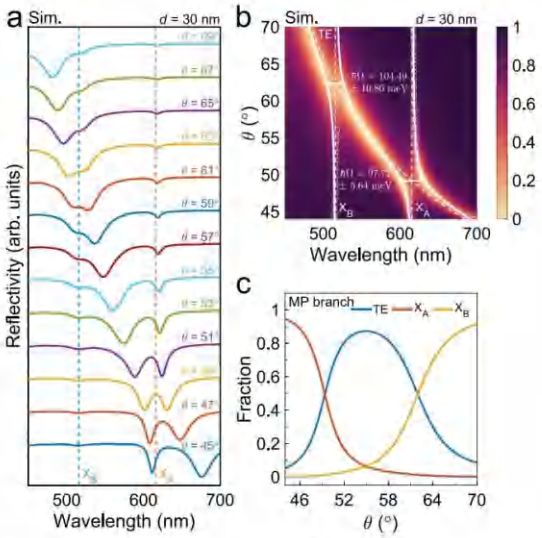


**Figure 2.** (a) Reflection spectra calculated for a $WS_2/Si_3N_4/Ag$ heterostructure ($d$ = 30 nm) at different incident angles. The resonance wavelengths of the A- and B-exciton are indicated by the vertical dashed lines. (b) Two-dimensional reflection spectra calculated for the $WS_2/Si_3N_4/Ag$ heterostructure with $d$ = 30 nm at different incident angles. The fittings of the dispersion relations for the polaritons (solid curves), which are manifested in the reflection spectra based on the Hamiltonian are also provided. The resonant wavelengths of the A- and B-exciton and the dispersion relation of the TE wave are indicated by dashed lines. The solid circles represent the dips in the reflection spectra. The Rabi splitting and its standard error are also provided. (c) Fractions of the TE wave, A-exciton, and B-exciton in the MP branch as a function of the incident angle.

existence of photon−exciton coupling. In this case, the dispersion relations of the polaritons can be described by the coupled oscillator model (COM), in which a Hamiltonian containing three oscillators are expressed as follows:

$$\hat{H} = \begin{pmatrix} E_{TE} - \frac{j\hbar\gamma_{TE}}{2} & g_{TE-A} & g_{TE-B} \\ g_{TE-A} & E_A - \frac{j\hbar\gamma_A}{2} & 0 \\ g_{TE-B} & 0 & E_B - \frac{j\hbar\gamma_B}{2} \end{pmatrix} \quad (1)$$

Here, $E_{TE}$, $E_A$, and $E_B$ are the resonant energies of the uncoupled TE wave, A-excitons, and B-excitons; $\gamma_{TE}$, $\gamma_A$, and $\gamma_B$ are the corresponding dissipation rates; $g_{TE-A}$ and $g_{TE-B}$ are the coupling strength between the TE wave and the A-excitons and that between the TE wave and the B-excitons. Since the two exciton resonances are well separated, there is no direct coupling between them (i.e., $g_{A-B} = 0$).

In Figure 2b, we present the fitting results for the dispersion relations of the polaritons based on the Hamiltonian. The energies of the A- and B-excitons used in the fitting are $E_A$ = 2. 014 eV and $E_B$ = 2. 404 eV, respectively. The Rabi splitting energies extracted from the fitting are $\hbar\Omega_{TE-A}$ = 97. 72 meV and $\hbar\Omega_{TE-B}$ = 104. 49 meV, respectively. The dissipation rates of the A- and B-exciton used in the fitting are $\hbar\gamma_A$ = 33 meV and $\hbar\gamma_B$ = 80 meV. Obviously, the strong coupling criterion $\hbar\Omega > \frac{1}{2}(\hbar\gamma_{TE} + \hbar\gamma_{ex})$ is fulfilled in both cases, implying that the photon−exciton coupling has entered into the strong coupling regime. When strong coupling occurs, the Hopfield coefficients obtained by the diagonalization of the Hamiltonian indicate the contributions of the TE wave and two excitons to the hybrid states. In Figure 2c, we show the fractions (Hopfield coefficients) of the TE wave and the two excitons in the middle polariton (MP) branch. It is interesting to observe non-negligible contributions from both the A-exciton (~6%) and B-exciton (~6%) at $\theta$ = 55°, indicating clearly the hybridization of the two excitons in the $WS_2$ monolayer mediated by the TE wave.

For comparison, we also calculated the two-dimensional reflection spectra for the $WS_2/Si_3N_4/Ag$ heterostructure ($d$ = 50 nm) at different incident angles, as shown in Figure S8. Similarly, one can also identify anticrossing behaviors around the A- and B-exciton, indicating the existence of photon−exciton coupling. However, the dispersion relations of the polaritons cannot be fitted well by using a Hamiltonian containing three oscillators. Instead, a Hamiltonian containing two oscillators is used to describe the coupling between the TE wave and the A-exciton (or B-exciton). We fitted the dispersion relations of the polaritons by using a Hamiltonian containing three oscillators and two oscillators (Supporting Information, Section S7). In the three-oscillator model, a large deviation of the fitting result from the simulation result is observed in the MP branch. In addition, the Rabi splitting extracted for the B-exciton is dramatically reduced to ~72.71 meV. We used the residual standard error (RSE) to characterize the deviation of the fitting results from the simulation results, defined as $\sqrt{\frac{\sum_{i=1}^{n}(y_i - \hat{y}_i)^2}{n-2}}$, where $y_i$ and $\hat{y}_i$ represent the simulation/experimental result and fitting result, respectively. It was found that the RSE of the three-oscillator model is much larger than that of the two-oscillator model. Apparently, the fitting based on the two-oscillator model appears to be much better. To simplify the three-oscillator model into a two-oscillator model, we set $g_{TE-B}$ = 0 for the coupling between the TE wave and the A-exciton and $g_{TE-A}$ = 0 for the coupling between the TE wave and the B-exciton. The Rabi splitting energies extracted from the fitting are $\hbar\Omega_{TE-A}$ = 103.79 meV and $\hbar\Omega_{TE-B}$ = 107.92 meV, which satisfy the strong coupling criterion in both cases. Notably, the TE wave cannot mediate the hybridization between the two excitons due to the narrow line width.

### 2.2. Effects of the LSPR of an Au Nanorod on the Coupling between the TE Wave and the Two Excitons.

In order to experimentally verify the hybridization of the two excitons mediated by the TE wave, we needed to measure the angled-resolved reflection spectra for the $WS_2/Si_3N_4/Ag$ heterostructure ($d$ = 30 nm). Since the size of the $WS_2$ monolayer is much smaller than that of the incident light beam, it remains a big challenge to carry out such measurements. As an alternative, we can introduce a nanoparticle on the $WS_2$ monolayer as the scatter to transfer the TE wave propagating on the surface into far-field radiation. In this work, we choose Au nanorods as the scatters for the TE wave. They can provide extra electric field enhancement which is beneficial to the coupling between the TE wave and the exciton.


https://doi.org/10.1021/acsanm.4c02981
ACS Appl. Nano Mater. XXXX, XXX, XXX−XXX

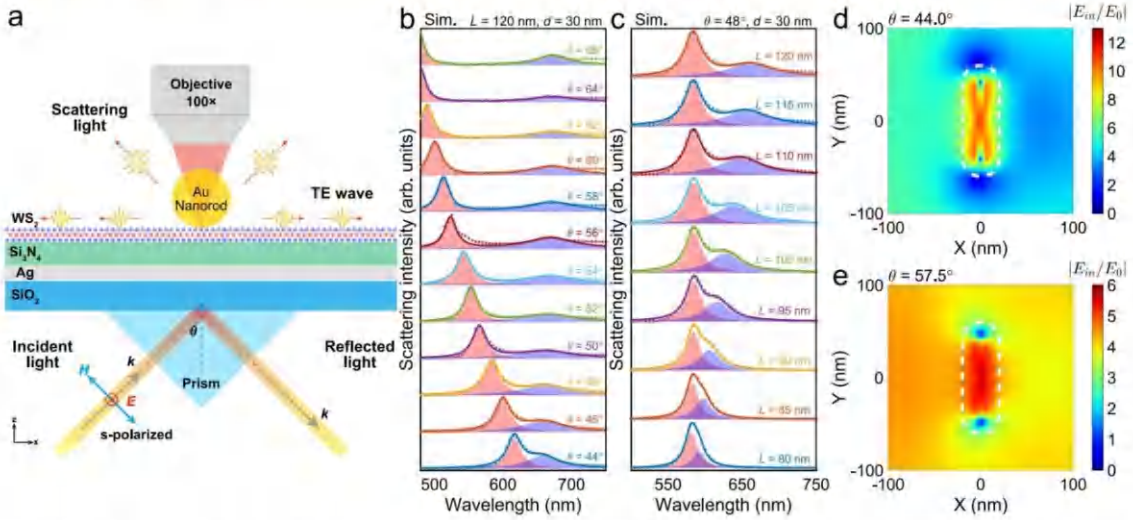


**Figure 3.** (a) Schematic showing the excitation of an Au nanorod placed on a $WS_2/Si_3N_4/Ag$ heterostructure by using the TE wave supported by the heterostructure and the detection of the TE wave scattered by the Au nanorod. The scattering spectra calculated for the Au nanorod placed on the $Si_3N_4/Ag$ heterostructure ($d$ = 30 nm) (b) at different incident angles (length fixed at $L$ = 120 nm) and (c) with different lengths (incident angle fixed at $\theta$ = 48°). The simulated scattering spectra based on the FEM are presented by solid circles. The solid curves represent the fitting results of the scattering spectra by using two Lorentzian line shapes; the red and blue shaded areas represent the contributions of the TE wave and the LSPR based on the fitting. The distributions of the in-plane electric field ($|E_{in}/E_0|$) on the surface of the $Si_3N_4$ layer at the resonant wavelengths of the A- and B-exciton for the $Si_3N_4/Ag$ heterostructure ($d$ = 30 nm) are presented in (d) and (e), respectively. In each case, the dashed curve shows the projection of the Au nanorod on the surface of the $Si_3N_4$ layer, and the incident angle is also provided.

In Figure 3a, we schematically show the use of a Au nanorod as a scatter to investigate the strong coupling between the TE wave and the two excitons in a $WS_2$ monolayer. Before doing that we needed to study the scattering properties of Au nanorods with different aspect ratios excited by the TE wave propagating on the $Si_3N_4/Ag$ heterostructure. The simulation results without the $WS_2$ monolayer are presented in Figure 3b–d.

We consider a Au nanorod with a length of $L$ = 120 nm placed on the $Si_3N_4/Ag$ heterostructure ($d$ = 30 nm). It is well-known that an Au nanorod supports a transverse surface plasmon resonance (TSPR) at a short wavelength and a longitudinal surface plasmon resonance (LSPR) at a long wavelength. In Figure 3b, we show the scattering spectra of the Au nanorod excited by using s-polarized light at different incident angles. Here, the polarization of the incident light is along the long axis of the Au nanorod. In all cases, one can observe two scattering peaks in the scattering spectra, which can be fitted with two Lorentzian line shapes. The scattering peak on the short-wavelength side exhibits a blue-shift with increasing incident angle. This behavior agrees with the feature of the TE wave. In contrast, the scattering peak on the long-wavelength side remains almost unchanged when the incident angle is varied. It originates from the LSPR of the Au nanorod. This assignment is confirmed by the scattering spectra of Au nanorods with different lengths (or aspect ratios) shown in Figure 3c. In this case, the incident angle is fixed at $\theta$ = 48°, and the polarization of the incident light is along the long axis of the Au nanorod. It is noticed that the scattering peak on the short-wavelength side, which corresponds to the TE wave, remains unchanged when the length of the Au nanorod is varied. In comparison, the scattering peak on the long-wavelength side exhibits a red-shift with increasing length of the Au nanorod.

It is noticed that the resonant energies and dissipation rates of the TE wave extracted from the scattering spectra are close to those derived from the reflection spectra, implying that the dissipation rate of the TE wave remains almost unchanged (Supporting Information, Section S8). We also examined the situation in which the Au nanorod is excited along the short axis (Supporting Information, Section S9). In this case, the TSPR of the Au nanorod is negligible because its intensity is much weaker than that of the TE wave. Therefore, we consider only the influence of the LSPR of an Au nanorod on the coupling between the TE wave and the two excitons.

In Figure 3d and 3e, we show the distributions of the in-plane electric field ($|E_{in}/E_0|$) on the surface of the $Si_3N_4/Ag$ heterostructure calculated for an Au nanorod ($L$ = 120 nm) at the resonant wavelengths of the A- and B-exciton, respectively. In this case, the in-plane electric field contains both the $x$- and $y$-components, which are defined as $|E_{in}| = \sqrt{|E_x|^2 + |E_y|^2}$. After introducing the Au nanorod, the in-plane electric field on the contact area between the Au nanorod and the $Si_3N_4$ layer is enhanced from ~5.22 to ~10.73 for the A-exciton and from ~4.41 to ~5.53 for the B-exciton, increasing the coupling between the TE wave and the two excitons (see the Supporting Information, Section S10).

When a Au nanorod is placed on the $WS_2/Si_3N_4/Ag$ heterostructure, we need to consider the coupling between the LSPR of the Au nanorod and the A-exciton because their resonant wavelengths are close to each other. In this case, the Hamiltonian composed of four oscillators is expressed as follows:


https://doi.org/10.1021/acsanm.4c02981
ACS Appl. Nano Mater. XXXX, XXX, XXX−XXX

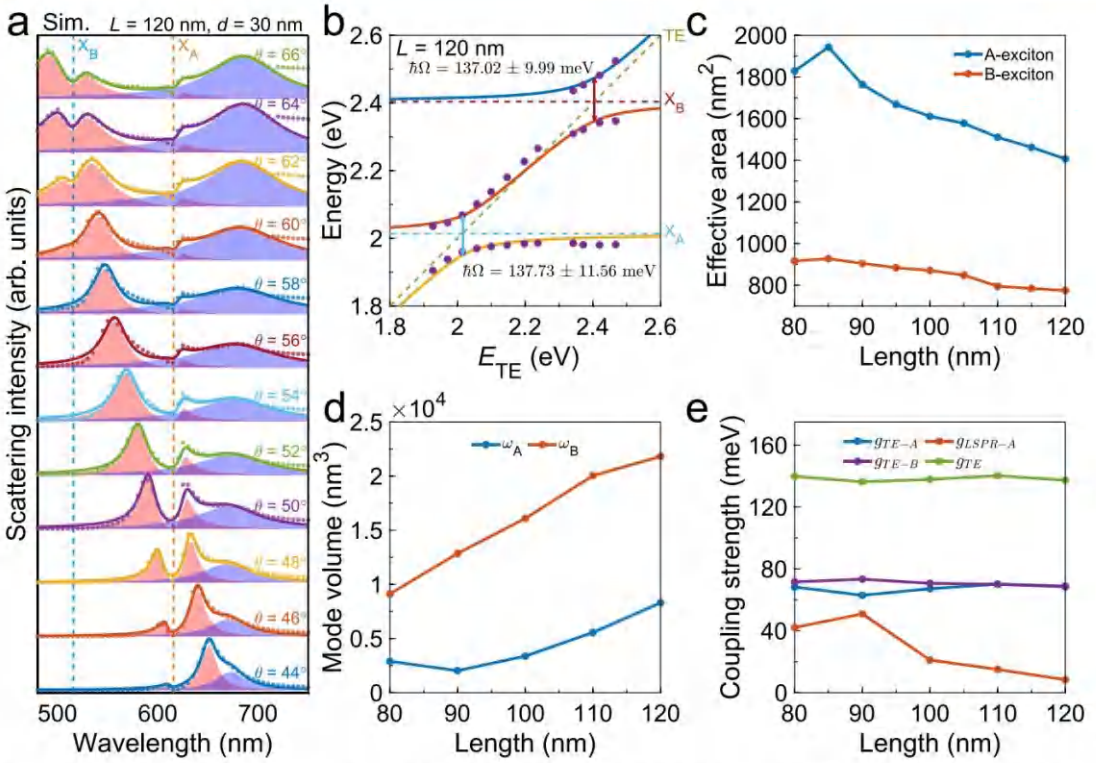


**Figure 4.** (a) Angle-resolved scattering spectra calculated for an Au nanorod ($L$ = 120 nm) placed on the $WS_2/Si_3N_4$/Ag heterostructure ($d$ = 30 nm). The simulated angle-resolved scattering spectra based on the FEM are represented by the solid circles, while the fitting results based on the COM are represented by solid curves. The contributions of the TE wave and LSPR are indicated by the red and blue shaded areas. The resonance wavelengths of A- and B-excitons are indicated by the vertical dashed lines. (b) Dispersion relations for the polaritons (solid circles) extracted from the angle-resolved scattering spectra shown in (a). The fittings for the dispersion relations (solid curves) based on Hamiltonian are also provided. The dispersion relation of the uncoupled TE wave and the energies of the two excitons are marked by dashed lines. The Rabi splitting and its standard error are also provided. The dependences of the effective area, mode volume of Au nanorod, and coupling strength on the length of the Au nanorod are presented in (c), (d), and (e), respectively.

$$\hat{H} = \begin{pmatrix} E_{TE} - \frac{j\hbar\gamma_{TE}}{2} & g_{TE-A} & g_{TE-B} & 0 \\ g_{TE-A} & E_A - \frac{j\hbar\gamma_A}{2} & 0 & g_{LSPR-A} \\ g_{TE-B} & 0 & E_B - \frac{j\hbar\gamma_B}{2} & 0 \\ 0 & g_{LSPR-A} & 0 & E_{LSPR} - \frac{j\hbar\gamma_{LSPR}}{2} \end{pmatrix} \quad (2)$$

Here, $E_{TE}$, $E_A$, $E_B$, and $E_{LSPR}$ are the resonant energies of the uncoupled TE wave, A-excitons, B-excitons, and LSPR, respectively; $\gamma_{TE}$, $\gamma_A$, $\gamma_B$, and $\gamma_{LSPR}$ are the corresponding dissipation rates; $g_{TE-A}$, $g_{TE-B}$, and $g_{LSPR-A}$ are the coupling strength between the TE wave and the A-excitons, that between the TE wave and the B-excitons, and that between the LSPR and the A-excitons. Since there is no coupling between the TE wave and the LSPR, we have $g_{TE-LSPR}$ = 0 (see the Supporting Information, Section S11).

In Figure 4a, we show the angle-resolved scattering spectra calculated for the Au nanorod ($L$ = 120 nm) placed on the $WS_2/Si_3N_4$/Ag heterostructure ($d$ = 30 nm) and excited using s-polarized light. In Figure 4b, we show the dispersion relations of the upper polariton (UP), MP, and lower polariton (LP) branches extracted from the scattering peaks in the angle-resolved scattering spectra shown in Figure 4a.

Basically, the angle-resolved scattering spectra can be fitted by using the expression of scattering intensity derived from the COM (Methods section), as shown by the solid curves in Figure 4a. Apart from the LSPR (blue shaded area), the other scattering peaks (red shaded areas) obtained by fitting correspond to the resonant energies of the hybrid states (i.e., UP, MP, and LP) (see solid circles in Figure 4b).

In the expression of scattering intensity (see the Methods section), the parameters that affect the scattering intensity of the Au nanorod include the resonant energies and line widths of the TE wave, the two excitons, the LSPR, the coupling strength between the TE wave and the two excitons, and the coupling strength between the LSPR and the A-exciton. The resonant energies and line widths of the TE wave, the two excitons, and the LSPR have been obtained from previous simulations and literatures. The coupling strength between the TE wave and the two excitons and that between the LSPR and the A-exciton can be derived from fitting the scattering spectra. With these parameters, the resonant energies of the UP, MP, and LP (solid curves in Figure 4b) can be derived by using the Hamiltonian containing three oscillators shown in eq 1.



https://doi.org/10.1021/acsanm.4c02981
ACS Appl. Nano Mater. XXXX, XXX, XXX−XXX

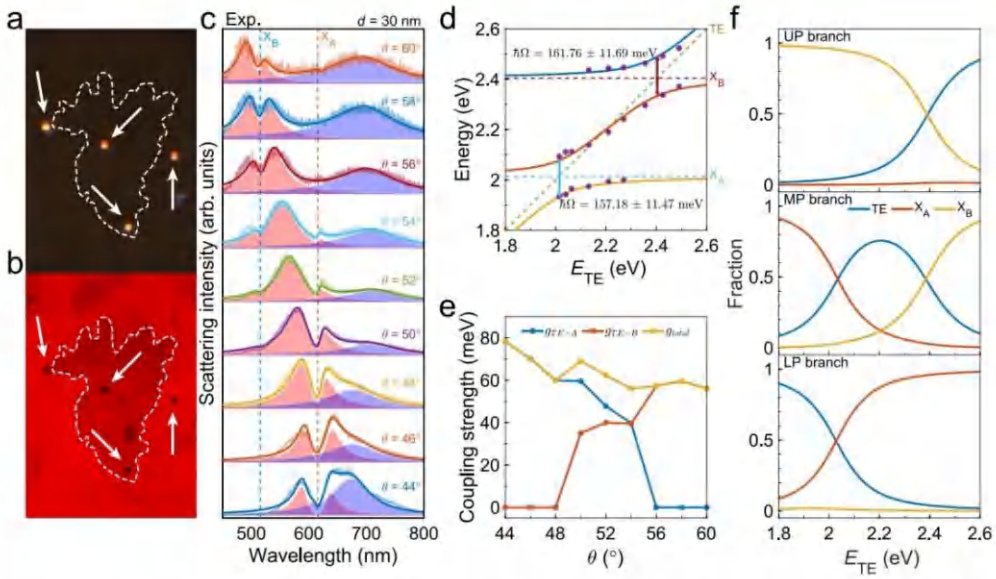


**Figure 5.** Dark-field (a) and bright-field (b) optical images of Au nanorod distributed on a $WS_2/Si_3N_4/Ag$ heterostructure. (c) Angle-resolved scattering spectra measured for an Au nanorod placed on the $WS_2/Si_3N_4/Ag$ heterostructure. The experimental measured angle-resolved scattering spectra are represented by the points, while the fitting results based on the COM are represented by solid curves. The contributions of the TE wave and LSPR are indicated by red and blue shaded areas. The resonance wavelengths of the A- and B-exciton are indicated by the vertical dashed lines. (d) Dispersion relations of the polaritons (solid circles) extracted from the scattering spectra shown in (c). The fittings of the dispersion relations (solid curves) based on Hamiltonian spectra are also provided. The dispersion relation of the uncoupled TE wave and the energies of the two excitons are marked by dashed lines. The Rabi splitting and its standard error are also provided. (e) Dependence of coupling strength ($g_{TE-A}$ and $g_{TE-B}$) and total coupling strength ($g_{total}$) on the incident angle. (f) Dependence of the fractions of the TE wave, A-exciton, and B-exciton in the UP, MP, and LP branches on the energy of the TE wave.

The Rabi splitting energies derived from fitting are found to be $\hbar\Omega_{TE-A}$ = 137.73 meV and $\hbar\Omega_{TE-B}$ = 137.02 meV. Apparently, the coupling strengths between the TE wave and the two excitons satisfy the strong coupling criterion, indicating that photon−exciton coupling in both cases has entered into the strong coupling regime.

We examined the influence of the length of the Au nanorod on the coupling strength. It was found that the coupling between the LSPR and the A-exciton is no longer in a strong coupling regime, and the coupling strength between the TE wave and the A-exciton exhibits a minimum for an Au nanorod with $L$ = 90 nm (see the Supporting Information, Section S12). Therefore, it is necessary to discuss the influence of the LSPR on the coupling strength between the TE wave and the A-exciton.

Basically, the coupling strength can be expressed as $g = \sqrt{N}\mu|E_{vac}|$. Here, $N$ is the number of excitons involved in the coupling, and $\mu$ is the transition dipole moment of the exciton. $|E_{vac}|$ represents the amplitude of the vacuum field, which is given by $|E_{vac}| = \sqrt{\hbar\omega/2\varepsilon_0\varepsilon_r V}$. Here, $\varepsilon_0$ is the vacuum permittivity, $\varepsilon_r$ is the dielectric constant, and $V$ is the mode volume. Thus, the coupling strength can be written as[18,25]

$$g = \mu\sqrt{\frac{N\hbar\omega}{2\varepsilon_0\varepsilon_r V}} \tag{3}$$

Apparently, the coupling strength will be affected by the number of excitons involved in coupling and the mode volume. Therefore, we need to discuss the influence of the LSPR on these two quantities.

In order to estimate the number of excitons involved in the coupling for a Au nanorod placed on the $WS_2/Si_3N_4/Ag$ heterostructure, we used a dipole source to excite the Au nanorod and examined the distribution of the radiation intensity around the Au nanorod. Physically, the radiation intensities at different positions around the Au nanorod reflect the number of excitons involved in the coupling, which can be positive or negative (Supporting Information, Section S13). If we defined an effective area ($S$) by integrating the radiation intensity over the projection of the Au nanorod, then the total number of excitons involved in the coupling can be estimated by using $S/A$, where $A$ is the size of the exciton (i.e., $N \propto S$).[25] In Figure 4c, we show the dependence of the effective area on the length of the Au nanorod at the two exciton resonances. For the A-exciton, the largest exciton number is observed in the Au nanorod with $L$ = 85 nm because the LSPR is close to the exciton resonance. For the B-exciton, the length of the Au nanorod (or LSPR) has little influence on the exciton number because it is far away from the exciton resonance.

In Figure 4d, we show the dependence of the mode volume of an Au nanorod at the exciton resonance on the length of the Au nanorod (see the Supporting Information, Section S14 for the calculation of mode volume[18,50]). For the A-exciton, the smallest mode volume is achieved when the LSPR of the Au nanorod is close to the A-exciton resonance. However, the variation of the mode volume around the A-exciton resonance is quite small. It increases gradually with an increasing length of the Au nanorod. For the B-exciton, the mode volume of the Au nanorod increases rapidly when the length of the Au nanorod increases.


https://doi.org/10.1021/acsanm.4c02981
ACS Appl. Nano Mater. XXXX, XXX, XXX−XXX

For a Au nanorod placed on the $WS_2/Si_3N_4/Ag$ heterostructure, the A-exciton couples not only with the TE wave but also with the LSPR. In comparison, the B-exciton couples only with the TE wave. In Figure 4e, we present the dependence of the coupling strength on the length of the Au nanorod calculated for the two excitons. Based on eq 3, the coupling strength between the TE wave and the A-exciton and that between the LSPR and the A-exciton depend mainly on the number of excitons involved in the coupling because the mode volumes of the TE wave and Au nanorod remain almost unchanged around the exciton resonance. In Figure 4c, it can be seen that the total number of excitons involved in the coupling reached a maximum value at the exciton resonance. Therefore, one can expect the strongest coupling strength (~50.94 meV) between the LSPR and the A-exciton in the Au nanorod with $L$ = 90 nm due to the enhanced electric field, as shown in Figure 4e. In contrast, the weakest coupling strength between the TE wave and the A-exciton is observed in this case. It implies that there exists a competition behavior for the coupling between the TE wave and A-exciton and that between the LSPR and the A-exciton. At the resonant wavelength of the A-exciton, more excitons are coupled to the LSPR of the Au nanorod, leading to a reduction in the coupling strength between the TE wave and the A-exciton. Thus, the strongest coupling between the TE and the A-exciton is observed in the Au nanorod ($L$ = 90 nm) which exhibits the largest enhancement factor for the in-plane electric field. Instead, the maximum coupling strength ($g_{TE} = g_{TE-A} + g_{TE-B}$) is achieved in the Au nanorod with $L$ = 110 nm. Since the LSPR is far away from the resonant wavelength of the B-exciton, the influence of the LSPR on the coupling between the TE wave and the B-exciton is negligible. Thus, the coupling strength between the TE wave and the B-exciton is not sensitive to the length of the Au nanorod (or LSPR).

We examined the dependence of $1/\sqrt{V}$ (or $\sqrt{S}$) on the coupling strength and observed a linear relationship between them, in agreement with eq 3 (see the Supporting Information, Section S15).

**2.3. Experimental Demonstration of the Hybridization of the A- and B-Exciton in a $WS_2$ Monolayer.** In our experiments, we used dark- and bright-field microscopes to characterize the Au nanorod placed on the $WS_2/Si_3N_4/Ag$ heterostructure, as shown in Figures 5a and 5b. The bright and dark spots in the optical images are individual Au nanorods distributed on the $WS_2$ monolayer. In the bright-field image, the gray area enclosed by the dashed curve corresponds to the $WS_2$ monolayer. In order to confirm the monolayer nature of $WS_2$, we performed photoluminescence (PL), Raman, and reflection spectra measurements for the $WS_2$ film attached on the $Si_3N_4/Ag$ heterostructure, as shown in Figure S19. The characteristics observed for the $WS_2$ film in the PL spectra and Raman spectra agree well with the previous reports.[51−53] In addition, the dissipation rate of the A-exciton was found be ~36.65 meV (see the Supporting Information, Section S16).

We measured the angle-resolved scattering spectra for the Au nanorod located on the $WS_2/Si_3N_4/Ag$ heterostructure ($d$ = 30 nm) (see the Supporting Information, Section S17, for the case with $d$ = 50 nm). Since the size of the Au nanorod is small, the signal-to-noise ratio in the measured scattering spectra is not so good at large incident angles when the TE wave is far from the LSPR of the Au nanorod (e.g., $\theta$ = 60°). However, one can still identify the scattering peaks in the scattering spectra. In order to accurately extract the resonant energies of the hybrid states, we first fitted the scattering spectra by using the expression of scattering intensity based on the COM (see the Methods section), as shown in Figure 5c. The measured scattering spectra are in good agreement with the simulated ones (Figure 4a). With increasing the incident angle, the resonant wavelength of the TE wave is blue-shifted. One can identify the anticrossing behaviors originating from the coupling between the TE wave and the two excitons. At $\theta$ = 52° and $\theta$ = 54°, one can see three scattering peaks and two scattering dips in the scattering spectra. It implies that the TE wave couples with the A- and B-exciton simultaneously. In Figure 5d, we show the UP, MP, and LP branches of the polaritons extracted from the angle-resolved scattering spectra. The fitting results based on Hamiltonian calculations are also provided. The Rabi splitting energies derived from the dispersion relations at the zero detuning are $\hbar\Omega_{TE-A}$ = 157.18 meV and $\hbar\Omega_{TE-B}$ = 161.76 meV. In both cases, the coupling strength between the TE wave and the exciton satisfies the strong coupling criterion. We extracted the coupling strengths $g_{TE-A}$ and $g_{TE-B}$ at nonzero detuning from the measured scattering spectra using the expression of scattering intensity (see the Methods section), as shown in Figure 5e. The total coupling strength ($g_{total}$), which is defined as $g_{total} = \sqrt{g_{TE-A}^2 + g_{TE-B}^2}$, was estimated to be ~62.29 meV at $\theta$ = 52°.[54] It is remarkable that an inflection point is observed in the MP branch when the energy is close to that of the uncoupled TE wave (see the dashed line). This is clear evidence for the hybridization of the two excitons mediated by the TE wave. In Figure 5f, we calculated the fractions of the TE wave and two excitons in the UP, MP, and LP branches. It can be seen that both the A- and B-exciton contribute ~12% to the MP branch at $\theta$ = 52°, which confirms undoubtedly the hybridization of the two excitons mediated by the TE wave.

Physically, the exciton hybridization is governed by the strong coupling between the TE wave and the two excitons and the dissipation rate of the TE wave. The use of Au nanorods as the scatters for the TE wave can greatly enhance the electric field, improving the strong coupling between the TE wave and the two excitons. In our simulation, the enhancement factors for the in-plane electric field at the wavelength of the A-exciton can be increased from ~5.22 to ~10.73 in the presence of an Au nanorod ($L$ = 120 nm). As a result, the Rabi splitting energy originating from the strong coupling between the TE wave and the A-exciton is increased from $\hbar\Omega_{TE-A}$ = 97.72 meV to $\hbar\Omega_{TE-A}$ = 137.73 meV in the presence of the Au nanorod. Similarly, the Rabi splitting energy arising from the strong coupling between the TE wave and the B-exciton is increased from $\hbar\Omega_{TE-B}$ = 104.49 meV to $\hbar\Omega_{TE-B}$ = 137.02 meV in the presence of the Au nanorod.

In the previous study, the Rabi splitting energies were found to be $\hbar\Omega_{TE-A}$ = 120.2 meV and $\hbar\Omega_{TE-B}$ = 139.7 meV by using a PS nanosphere are the scatters.[49] In this work, the Rabi splitting energies extracted from the experimental data were found to be $\hbar\Omega_{TE-A}$ = 157.18 meV and $\hbar\Omega_{TE-B}$ = 161.76 meV when a Au nanorod was used as the scatter (see Figure 5d). These results indicate clearly that the use of Au nanorods as the scatters can enhance the strong coupling between the TE wave and the two excitons, facilitating the exciton hybridization. As demonstrated in this work, the exciton hybridization is improved in the presence of an Au nanorod. The contribution of the A- or B-exciton in the MP branch is increased from ~6% (see Figure 2c) to ~12% (see Figure 5f).



https://doi.org/10.1021/acsanm.4c02981
ACS Appl. Nano Mater. XXXX, XXX, XXX−XXX

In the numerical simulations described above, we assumed a gap width of 1.0 nm between the Au nanorod and the $WS_2$ monolayer. In Figure S21, we show the in-plane electric field distribution ($|E_{in}/E_0|$) calculated for an Au nanorod placed on the $Si_3N_4$/Ag heterostructure with a gap width of 0.5 nm. It was found that the enhancement factors can be further enhanced from ~10.73 to ~12.31 for the A-exciton and from ~5.53 to ~5.94 for the B-exciton (Supporting Information, Section S18). In our experiments, the gap width between the Au nanorod and the $WS_2$ monolayer might be smaller than 1.0 nm, leading to an enhanced electric field and a stronger coupling strength. This is the reason that the Rabi splitting energies extracted from the experiment data are larger than the simulation results.

## 3. CONCLUSION

In summary, we investigated the influence of the thickness of the Ag film in a $Si_3N_4$/Ag heterostructure on the dissipation rate of the TE wave supported by the heterostructure. It was found that the hybridization of the A- and B-excitons in a $WS_2$ monolayer attached on the $Si_3N_4$/Ag heterostructure can be realized by appropriately choosing the thickness of the Ag film. We numerically simulated the angle-resolved reflection spectra of the $WS_2/Si_3N_4$/Ag heterostructure and demonstrated the hybridization of the A- and B-exciton mediated by the TE wave. In experiments, we introduced Au nanorods as scatterers for the TE wave, which enhance the in-plane electric field and achieve stronger photon−exciton coupling. We experimentally measured the angle-resolved scattering spectra for an Au nanorod placed on the $WS_2/Si_3N_4$/Ag heterostructure. We demonstrated the strong coupling between the TE wave and the two excitons and confirmed the hybridization of the A- and B-excitons mediated by the TE wave.

The advantages of the system studied in this work include:

1. It enables the realization of the hybridization of the two excitons in the same material, in contrast to the hybridization of the exciton in different excitonic materials.
2. It will deepen the understanding of strong coupling because the two excitons in $WS_2$ monolayer are well separated (~390 meV) as compared with other excitonic materials.
3. The dispersion relations of the polaritons can be extracted by simply changing the incident angle.
4. This system is functional at room temperature because of the large binding energies of the two excitons in $WS_2$ monolayer.
5. It can be constructed the photonic and plasmonic devices by exploiting the energy exchange between the two excitons.

Our findings open horizons for realizing and manipulating strong light−matter interactions in two-dimensional materials and pave the way for the construction of photonic and plasmonic devices by exploiting dielectric−metal heterostructures.

## 4. METHODS

**4.1. Sample Preparation.** The $WS_2/Si_3N_4$/Ag heterostructures used in this work were fabricated using the following procedure. First, a Ag film was coated on a $SiO_2$ substrate by using electron beam evaporation. Then, a $Si_3N_4$ layer was deposited on the Ag film via high-frequency plasma-enhanced chemical vapor deposition (HF-PECVD). The thickness of the $Si_3N_4$ layer was controlled by the deposition time. The $WS_2$ monolayers were first synthesized on a Si substrate via chemical vapor deposition (CVD) method and then transferred onto a $Si_3N_4$/Ag heterostructure by a wet-transfer approach, forming $WS_2/Si_3N_4$/Ag heterostructure. The aqueous solution of Au nanorods was dropped onto the $WS_2/Si_3N_4$/Ag heterostructure and dried naturally.

**4.2. Optical Characterization.** A home-built coupling system was used to generate the TE waves on the surface of the $Si_3N_4$/Ag heterostructure via the Kretschmann−Raether configuration. The sample was mounted on a prism made of $SiO_2$ (K9 glass) with silicone oil whose refractive index was close to that of $SiO_2$. Collimated s-polarized white light delivered by a multimode optical fiber was used as the excitation source. The scattering light of Au nanorods on the $WS_2/Si_3N_4$/Ag heterostructure was collected by using the objective (100×, NA = 0.85) of an inverted dark-field microscope (Axio Observer A1, Zeiss) for analysis and imaging. The scattering spectra were analyzed by using a spectrometer (SR-500i-B1, Andor), and the images of scattering light were recorded by using a color charge coupled device (CCD) (DS-Ri2, Nikon).

**4.3. Numerical Simulations.** In principle, the Maxwell equations can be solved in both frequency domains and time domains, commonly utilizing the finite element method (FEM) and the finite-difference time-domain (FDTD) method. However, when the light source is obliquely incident, FDTD requires more computational time than FEM. On the other hand, dipole source can be more easily implemented in FDTD simulations. Therefore, choosing the appropriate method can significantly improve the simulation efficiency. In our study, we calculated the reflection spectra for the $Si_3N_4$/Ag and $WS_2/Si_3N_4$/Ag heterostructure as well as the scattering spectra of an Au nanorod placed on the $Si_3N_4$/Ag and $WS_2/Si_3N_4$/Ag heterostructure via FEM (COMSOL Multiphysics v5.6). Additionally, we employed the FDTD method (FDTD Solutions, Lumerical) to calculate the radiation intensity distribution of the Au nanorod placed on the $WS_2/Si_3N_4$/Ag heterostructure using a dipole source.

In the numerical simulations, the Au nanorod was modeled as a cylinder capped with a hemisphere at each end. The lengths and diameters of the Au nanorods were set to $L$ and 40 nm, respectively. The $Si_3N_4$/Ag heterostructure was modeled as a layered structure, where the thickness of the $Si_3N_4$ layer and Ag film were set to 75 nm and $d$, respectively. The thickness of the $WS_2$ monolayer was set at 1.0 nm. The $SiO_2$ substrate was modeled as a semi-infinite dielectric substrate. The gap between Au nanorod and the surface of the $Si_3N_4$/Ag heterostructure or $WS_2/Si_3N_4$/Ag heterostructure was set to be 1.0 nm. The dielectric constants for Au and Ag were taken from Johnson and Christy.[55] The dielectric constants for the $WS_2$ monolayer, $Si_3N_4$ layer, and $SiO_2$ substrate were taken from the literature[56−58] (see the Supporting Information, Section S1, for more details).

**4.4. Coupled Oscillator Model.** In order to extract the coupling parameters through the fitting of the scattering spectra, the coupling system can be described as coupled harmonic oscillators with the following motion equations:[40,59,60]

$$\ddot{x}_m(t) + \gamma_m \dot{x}_m(t) + \omega_m^2 x_m(t) + 2\sum_{n=1}^{N} \varepsilon_{mn} g_{mn} \dot{x}_n(t) = F_m(t)$$

where $m$ and $n$ = TE, A, B, and LSPR stand for the indices of the four resonances; $x_m$, $\omega_m$, and $\gamma_m$ are the amplitude, angular frequency, and dissipation rate of the $m$th oscillator; $g_{mn}$ is the coupling strength between the $m$th and $n$th oscillator; $F_m(t)$ is the driving force for the $m$th oscillator induced by external light field; and $\varepsilon_{mn}$ is the Levi−Civita symbol, which is defined as[40]

$$\varepsilon_{mn} = \begin{cases} +1, & m < n \\ 0, & m = n \\ -1, & m > n \end{cases}$$

Under a harmonic driving force of external light field $F_m(t) = F_m e^{-j\omega t}$, the motion equations can be simplified as the steady-state equations:

$$(\omega_m^2 - j\omega\gamma_m - \omega^2)x_m - 2j\omega \sum_{n=1}^{N} \varepsilon_m g_{mn} x_n = F_m$$

For the four oscillators, only the TE wave and the LSPR can be predominately excited by the external light field, which means that $F_A = 0$ and $F_B = 0$. By solving the steady-state equations, we can obtain the amplitude of the TE wave and LSPR (see the Supporting Information, Section S2, for more details).

According to the Larmor formula of the dipole radiation, the intensity of the scattering light reads[60]

$$I_{scat} \propto \omega^4 |x_{TE}|^2 + \omega^4 |x_{LSPR}|^2$$

It means that the scattering spectra of the Au nanorod placed on the $WS_2/Si_3N_4/Ag$ heterostructure is composed of the contributions of the TE wave and the LSPR.

Based on the expression of scattering intensity, the calculated and measured scattering spectra of the Au nanorod placed on the $WS_2/Si_3N_4/Ag$ heterostructure can be fitted by the Levenberg–Marquardt algorithm using MATLAB software, thereby enabling the extraction of coupling parameters.

## ■ ASSOCIATED CONTENT

### Supporting Information

The Supporting Information is available free of charge at https://pubs.acs.org/doi/10.1021/acsanm.4c02981.

Detailed information about the numerical simulation settings in COMSOL and FDTD; reflection spectra calculated for $Si_3N_4/Ag$ heterostructure and $WS_2/Si_3N_4/Ag$ heterostructure, both composed of Ag films with different thicknesses; electric field distributions calculated for the $Si_3N_4/Ag$ heterostructure and an Au nanorod placed on the $Si_3N_4/Ag$ heterostructure; scattering spectra calculated for Au nanorods and corresponding dispersion relations of the polaritons; radiation distribution of a dipole source via an Au nanorod; mode volume of an Au nanorod with the relationship between the number of excitons and coupling strength (PDF)

## ■ AUTHOR INFORMATION


### Corresponding Author

**Sheng Lan** − *Guangdong Provincial Key Laboratory of Nanophotonic Functional Materials and Devices, School of Information and Optoelectronic Science and Engineering, South China Normal University, Guangzhou 510006, China;* orcid.org/0000-0002-7277-0042; Email: slan@scnu.edu.cn

### Authors

**Weichen He** − *Guangdong Provincial Key Laboratory of Nanophotonic Functional Materials and Devices, School of Information and Optoelectronic Science and Engineering, South China Normal University, Guangzhou 510006, China;* orcid.org/0000-0003-0718-5063

**Shimei Liu** − *Guangdong Provincial Key Laboratory of Nanophotonic Functional Materials and Devices, School of Information and Optoelectronic Science and Engineering, South China Normal University, Guangzhou 510006, China;* orcid.org/0000-0001-5704-095X

**Jingting Liu** − *Guangdong Provincial Key Laboratory of Nanophotonic Functional Materials and Devices, School of Information and Optoelectronic Science and Engineering, South China Normal University, Guangzhou 510006, China;* orcid.org/0009-0007-5796-810X

**Shulei Li** − *Guangdong Provincial Key Laboratory of Nanophotonic Functional Materials and Devices, School of Information and Optoelectronic Science and Engineering, South China Normal University, Guangzhou 510006, China; School of Optoelectronic Engineering, Guangdong Polytechnic Normal University, Guangzhou 510665, China*

**Fu Deng** − *Department of Physics, The Hong Kong University of Science and Technology, Hong Kong 999077, China*

**Haiying Liu** − *Guangdong Provincial Key Laboratory of Nanophotonic Functional Materials and Devices, School of Information and Optoelectronic Science and Engineering, South China Normal University, Guangzhou 510006, China*

**Haihua Fan** − *Guangdong Provincial Key Laboratory of Nanophotonic Functional Materials and Devices, School of Information and Optoelectronic Science and Engineering, South China Normal University, Guangzhou 510006, China*

**Jun Dai** − *School of Optoelectronic Engineering, Guangdong Polytechnic Normal University, Guangzhou 510665, China*

Complete contact information is available at: https://pubs.acs.org/10.1021/acsanm.4c02981


### Author Contributions

W. He and S. Liu contributed equally to this work. W. He, S. Li, and S. Lan conceived the idea; W. He and J. Liu performed the numerical simulations; W. He and S. Li fabricated the samples; W. He, S. Liu, and J. Liu carried out the optical measurements; W. He, S. Liu, F. Deng, H. Liu, H. Fan, J. Dai, and S. Lan analyzed the data and wrote the manuscript; S. Lan supervised the project. All of the authors read and commented on the manuscript.

### Notes

The authors declare no competing financial interest.

## ■ ACKNOWLEDGMENTS

S.L. acknowledges financial support from the National Natural Science Foundation of China (Grant Nos. 12174123 and 12374347). S.L. acknowledges financial support from the Guangdong Basic and Applied Basic Research Foundation (Grant No. 2022A1515010747). This work was financially supported by the Scientific Research Innovation Project of Graduate School of South China Normal University.

## ■ REFERENCES


(1) Vasa, P.; Wang, W.; Pomraenke, R.; Lammers, M.; Maiuri, M.; Manzoni, C.; Cerullo, G.; Lienau, C. Real-Time Observation of Ultrafast Rabi Oscillations between Excitons and Plasmons in Metal Nanostructures with J-Aggregates. *Nat. Photonics* **2013**, *7*, 128−132.

(2) Ramezani, M.; Halpin, A.; Fernández-Domínguez, A. I.; Feist, J.; Rodriguez, S. R.-K.; Garcia-Vidal, F. J.; Rivas, J. G. Plasmon−Exciton−Polariton Lasing. *Optica* **2017**, *4*, 31−37.

(3) Peng, P.; Liu, Y.-C.; Xu, D.; Cao, Q.-T.; Lu, G.; Gong, Q.; Xiao, Y.-F. Enhancing Coherent Light-Matter Interactions through Microcavity-Engineered Plasmonic Resonances. *Phys. Rev. Lett.* **2017**, *119*, 233901.

(4) Törmä, P.; Barnes, W. L. Strong Coupling between Surface Plasmon Polaritons and Emitters: A Review. *Rep. Prog. Phys.* **2015**, *78*, 013901.

(5) Frisk Kockum, A.; Miranowicz, A.; De Liberato, S.; Savasta, S.; Nori, F. Ultrastrong Coupling between Light and Matter. *Nat. Rev. Phys.* **2019**, *1*, 19−40.

(6) Lidzey, D. G.; Bradley, D. D. C.; Armitage, A.; Walker, S.; Skolnick, M. S. Photon-Mediated Hybridization of Frenkel Excitons in Organic Semiconductor Microcavities. *Science* **2000**, *288*, 1620−1623.

(7) Kang, H.; Ma, J.; Li, J.; Zhang, X.; Liu, X. Exciton Polaritons in Emergent Two-Dimensional Semiconductors. *ACS Nano* **2023**, *17*, 24449−24467.
(8) Holmes, R. J.; Kéna-Cohen, S.; Menon, V. M.; Forrest, S. R. Strong Coupling and Hybridization of Frenkel and Wannier-Mott Excitons in an Organic-Inorganic Optical Microcavity. *Phys. Rev. B* **2006**, *74*, 235211.
(9) Wenus, J.; Parashkov, R.; Ceccarelli, S.; Brehier, A.; Lauret, J.-S.; Skolnick, M. S.; Deleporte, E.; Lidzey, D. G. Hybrid Organic-Inorganic Exciton-Polaritons in a Strongly Coupled Microcavity. *Phys. Rev. B* **2006**, *74*, 235212.
(10) Coles, D. M.; Somaschi, N.; Michetti, P.; Clark, C.; Lagoudakis, P. G.; Savvidis, P. G.; Lidzey, D. G. Polariton-Mediated Energy Transfer between Organic Dyes in a Strongly Coupled Optical Microcavity. *Nat. Mater.* **2014**, *13*, 712−719.
(11) Georgiou, K.; Michetti, P.; Gai, L.; Cavazzini, M.; Shen, Z.; Lidzey, D. G. Control over Energy Transfer between Fluorescent BODIPY Dyes in a Strongly Coupled Microcavity. *ACS Photonics* **2018**, *5*, 258−266.
(12) Zhong, X.; Chervy, T.; Zhang, L.; Thomas, A.; George, J.; Genet, C.; Hutchison, J. A.; Ebbesen, T. W. Energy Transfer Between Spatially Separated Entangled Molecules. *Angew. Chem.* **2017**, *129*, 9162−9166.
(13) Georgiou, K.; Jayaprakash, R.; Othonos, A.; Lidzey, D. G. Ultralong-Range Polariton-Assisted Energy Transfer in Organic Microcavities. *Angew. Chem.* **2021**, *133*, 16797−16803.
(14) Zengin, G.; Wersäll, M.; Nilsson, S.; Antosiewicz, T. J.; Käll, M.; Shegai, T. Realizing Strong Light-Matter Interactions between Single-Nanoparticle Plasmons and Molecular Excitons at Ambient Conditions. *Phys. Rev. Lett.* **2015**, *114*, 157401.
(15) Wang, H.; Ke, Y.; Xu, N.; Zhan, R.; Zheng, Z.; Wen, J.; Yan, J.; Liu, P.; Chen, J.; She, J.; Zhang, Y.; Liu, F.; Chen, H.; Deng, S. Resonance Coupling in Silicon Nanosphere-J-Aggregate Heterostructures. *Nano Lett.* **2016**, *16*, 6886−6895.
(16) Wersäll, M.; Cuadra, J.; Antosiewicz, T. J.; Balci, S.; Shegai, T. Observation of Mode Splitting in Photoluminescence of Individual Plasmonic Nanoparticles Strongly Coupled to Molecular Excitons. *Nano Lett.* **2017**, *17*, 551−558.
(17) Wersäll, M.; Munkhbat, B.; Baranov, D. G.; Herrera, F.; Cao, J.; Antosiewicz, T. J.; Shegai, T. Correlative Dark-field and Photoluminescence Spectroscopy of Individual Plasmon-Molecule Hybrid Nanostructures in a Strong Coupling Regime. *ACS Photonics* **2019**, *6*, 2570−2576.
(18) Chikkaraddy, R.; de Nijs, B.; Benz, F.; Barrow, S. J.; Scherman, O. A.; Rosta, E.; Demetriadou, A.; Fox, P.; Hess, O.; Baumberg, J. J. Single-Molecule Strong Coupling at Room Temperature in Plasmonic Nanocavities. *Nature* **2016**, *535*, 127−130.
(19) Savasta, S.; Saija, R.; Ridolfo, A.; Di Stefano, O.; Denti, P.; Borghese, F. Nanopolaritons: Vacuum Rabi Splitting with a Single Quantum Dot in the Center of a Dimer Nanoantenna. *ACS Nano* **2010**, *4*, 6369−6376.
(20) Zhou, N.; Yuan, M.; Gao, Y.; Li, D.; Yang, D. Silver Nanoshell Plasmonically Controlled Emission of Semiconductor Quantum Dots in the Strong Coupling Regime. *ACS Nano* **2016**, *10*, 4154−4163.
(21) Santhosh, K.; Bitton, O.; Chuntonov, L.; Haran, G. Vacuum Rabi Splitting in a Plasmonic Cavity at the Single Quantum Emitter Limit. *Nat. Commun.* **2016**, *7*, ncomms11823.
(22) Liu, R.; Zhou, Z.-K.; Yu, Y.-C.; Zhang, T.; Wang, H.; Liu, G.; Wei, Y.; Chen, H.; Wang, X.-H. Strong Light-Matter Interactions in Single Open Plasmonic Nanocavities at the Quantum Optics Limit. *Phys. Rev. Lett.* **2017**, *118*, 237401.
(23) Ramasubramaniam, A. Large Excitonic Effects in Monolayers of Molybdenum and Tungsten Dichalcogenides. *Phys. Rev. B* **2012**, *86*, 115409.
(24) Sie, E. J.; McIver, J. W.; Lee, Y.-H.; Fu, L.; Kong, J.; Gedik, N. Valley-Selective Optical Stark Effect in Monolayer $WS_2$. *Nat. Mater.* **2015**, *14*, 290−294.
(25) Wen, J.; Wang, H.; Wang, W.; Deng, Z.; Zhuang, C.; Zhang, Y.; Liu, F.; She, J.; Chen, J.; Chen, H.; Deng, S.; Xu, N. Room-Temperature Strong Light-Matter Interaction with Active Control in Single Plasmonic Nanorod Coupled with Two-Dimensional Atomic Crystals. *Nano Lett.* **2017**, *17*, 4689−4697.
(26) Jiang, Y.; Wang, H.; Wen, S.; Chen, H.; Deng, S. Resonance Coupling in an Individual Gold Nanorod-Monolayer $WS_2$ Heterostructure: Photoluminescence Enhancement with Spectral Broadening. *ACS Nano* **2020**, *14*, 13841−13851.
(27) Zheng, D.; Zhang, S.; Deng, Q.; Kang, M.; Nordlander, P.; Xu, H. Manipulating Coherent Plasmon-Exciton Interaction in a Single Silver Nanorod on Monolayer $WSe_2$. *Nano Lett.* **2017**, *17*, 3809−3814.
(28) Cuadra, J.; Baranov, D. G.; Wersall, M.; Verre, R.; Antosiewicz, T. J.; Shegai, T. Observation of Tunable Charged Exciton Polaritons in Hybrid Monolayer $WS_2$-Plasmonic Nanoantenna System. *Nano Lett.* **2018**, *18*, 1777−1785.
(29) Yankovich, A. B.; Munkhbat, B.; Baranov, D. G.; Cuadra, J.; Olsén, E.; Lourenço-Martins, H.; Tizei, L. H. G.; Kociak, M.; Olsson, E.; Shegai, T. Visualizing Spatial Variations of Plasmon-Exciton Polaritons at the Nanoscale Using Electron Microscopy. *Nano Lett.* **2019**, *19*, 8171−8181.
(30) Munkhbat, B.; Baranov, D. G.; Bisht, A.; Hoque, M. A.; Karpiak, B.; Dash, S. P.; Shegai, T. Electrical Control of Hybrid Monolayer Tungsten Disulfide-Plasmonic Nanoantenna Light-Matter States at Cryogenic and Room Temperatures. *ACS Nano* **2020**, *14*, 1196−1206.
(31) Deng, F.; Huang, H.; Chen, J.-D.; Liu, S.; Pang, H.; He, X.; Lan, S. Greatly Enhanced Plasmon-Exciton Coupling in Si/$WS_2$/Au Nanocavities. *Nano Lett.* **2022**, *22*, 220−228.
(32) Liu, S.; Deng, F.; Zhuang, W.; He, X.; Huang, H.; Chen, J.-D.; Pang, H.; Lan, S. Optical Introduction and Manipulation of Plasmon-Exciton-Trion Coupling in a Si/$WS_2$/Au Nanocavity. *ACS Nano* **2022**, *16*, 14390−14401.
(33) Kleemann, M.-E.; Chikkaraddy, R.; Alexeev, E. M.; Kos, D.; Carnegie, C.; Deacon, W.; De Pury, A. C.; Große, C.; De Nijs, B.; Mertens, J.; Tartakovskii, A. I.; Baumberg, J. J. Strong-Coupling of $WSe_2$ in Ultra-Compact Plasmonic Nanocavities at Room Temperature. *Nat. Commun.* **2017**, *8*, 1296.
(34) Lassiter, J. B.; McGuire, F.; Mock, J. J.; Ciraci, C.; Hill, R. T.; Wiley, B. J.; Chilkoti, A.; Smith, D. R. Plasmonic Waveguide Modes of Film-Coupled Metallic Nanocubes. *Nano Lett.* **2013**, *13*, 5866−5872.
(35) Sun, J.; Hu, H.; Zheng, D.; Zhang, D.; Deng, Q.; Zhang, S.; Xu, H. Light-Emitting Plexciton: Exploiting Plasmon-Exciton Interaction in the Intermediate Coupling Regime. *ACS Nano* **2018**, *12*, 10393−10402.
(36) Han, X.; Wang, K.; Xing, X.; Wang, M.; Lu, P. Rabi Splitting in a Plasmonic Nanocavity Coupled to a $WS_2$ Monolayer at Room Temperature. *ACS Photonics* **2018**, *5*, 3970−3976.
(37) Hou, S.; Tobing, L. Y. M.; Wang, X.; Xie, Z.; Yu, J.; Zhou, J.; Zhang, D.; Dang, C.; Coquet, P.; Tay, B. K.; Birowosuto, M. D.; Teo, E. H. T.; Wang, H. Manipulating Coherent Light-Matter Interaction: Continuous Transition between Strong Coupling and Weak Coupling in $MoS_2$ Monolayer Coupled with Plasmonic Nanocavities. *Adv. Opt. Mater.* **2019**, *7*, 1900857.
(38) Wang, S.; Li, S.; Chervy, T.; Shalabney, A.; Azzini, S.; Orgiu, E.; Hutchison, J. A.; Genet, C.; Samorì, P.; Ebbesen, T. W. Coherent Coupling of $WS_2$ Monolayers with Metallic Photonic Nanostructures at Room Temperature. *Nano Lett.* **2016**, *16*, 4368−4374.
(39) Liu, W.; Lee, B.; Naylor, C. H.; Ee, H.-S.; Park, J.; Johnson, A. T. C.; Agarwal, R. Strong Exciton-Plasmon Coupling in $MoS_2$ Coupled with Plasmonic Lattice. *Nano Lett.* **2016**, *16*, 1262−1269.
(40) Liu, W.; Wang, Y.; Naylor, C. H.; Lee, B.; Zheng, B.; Liu, G.; Johnson, A. T. C.; Pan, A.; Agarwal, R. Understanding the Different Exciton-Plasmon Coupling Regimes in Two-Dimensional Semiconductors Coupled with Plasmonic Lattices: A Combined Experimental and Unified Equation of Motion Approach. *ACS Photonics* **2018**, *5*, 192−204.
(41) Li, B.; Zu, S.; Zhang, Z.; Zheng, L.; Jiang, Q.; Du, B.; Luo, Y.; Gong, Y.; Zhang, Y.; Lin, F.; Shen, B.; Zhu, X.; Ajayan, P. M.; Fang, Z. Large Rabi Splitting Obtained in Ag-$Ws_2$ Strong-Coupling Hetero-


https://doi.org/10.1021/acsanm.4c02981
ACS Appl. Nano Mater. XXXX, XXX, XXX−XXX

structure with Optical Microcavity at Room Temperature. *Opto-Electron. Adv.* **2019**, *2*, 19000801.
(42) Du, W.; Zhao, J.; Zhao, W.; Zhang, S.; Xu, H.; Xiong, Q. Ultrafast Modulation of Exciton-Plasmon Coupling in a Monolayer $WS_2$-Ag Nanodisk Hybrid System. *ACS Photonics* **2019**, *6*, 2832−2840.
(43) Wang, H.; Wen, J.; Wang, W.; Xu, N.; Liu, P.; Yan, J.; Chen, H.; Deng, S. Resonance Coupling in Heterostructures Composed of Silicon Nanosphere and Monolayer $WS_2$: A Magnetic-Dipole-Mediated Energy Transfer Process. *ACS Nano* **2019**, *13*, 1739−1750.
(44) Lepeshov, S.; Wang, M.; Krasnok, A.; Kotov, O.; Zhang, T.; Liu, H.; Jiang, T.; Korgel, B.; Terrones, M.; Zheng, Y.; Alú, A. Tunable Resonance Coupling in Single Si Nanoparticle-Monolayer $WS_2$ Structures. *ACS Appl. Mater. Interfaces* **2018**, *10*, 16690−16697.
(45) Liu, X.; Galfsky, T.; Sun, Z.; Xia, F.; Lin, E.-c.; Lee, Y.-H.; Kéna-Cohen, S.; Menon, V. M. Strong Light-Matter Coupling in Two-Dimensional Atomic Crystals. *Nat. Photonics* **2015**, *9*, 30−34.
(46) Deng, F.; Liu, H.; Xu, L.; Lan, S.; Miroshnichenko, A. E. Strong Exciton-Plasmon Coupling in a $WS_2$ Monolayer on Au Film Hybrid Structures Mediated by Liquid Ga Nanoparticles. *Laser Photonics Rev.* **2020**, *14*, 1900420.
(47) Li, S.; Zhou, L.; Panmai, M.; Xiang, J.; Lan, S. Magnetic Plasmons Induced in a Dielectric-Metal Heterostructure by Optical Magnetism. *Nanophotonics* **2021**, *10*, 2639−2649.
(48) Rose, A. H.; Dunklin, J. R.; Zhang, H.; Merlo, J. M.; van de Lagemaat, J. Plasmon-Mediated Coherent Superposition of Discrete Excitons under Strong Exciton-Plasmon Coupling in Few-Layer $MoS_2$ at Room Temperature. *ACS Photonics* **2020**, *7*, 1129−1134.
(49) Li, S.; Zhou, L.; Deng, F.; Xiang, J.; Panmai, M.; Huang, H.; Li, G.; Chen, J.; Lan, S. Transverse-Electric-Polarized Polaritons Propagating in a $WS_2/Si_3N_4$/Ag Heterostructure. *Laser Photonics Rev.* **2022**, *16*, 2100457.
(50) Yang, L.; et al. Strong Light-Matter Interactions between Gap Plasmons and Two-Dimensional Excitons under Ambient Conditions in a Deterministic Way. *Nano Lett.* **2022**, *22*, 2177−2186.
(51) Berkdemir, A.; Gutiérrez, H. R.; Botello-Méndez, A. R.; Perea-López, N.; Elías, A. L.; Chia, C.-I.; Wang, B.; Crespi, V. H.; López-Urías, F.; Charlier, J.-C.; Terrones, H.; Terrones, M. Identification of Individual and Few Layers of $WS_2$ Using Raman Spectroscopy. *Sci. Rep.* **2013**, *3*, 1755.
(52) McCreary, K. M.; Hanbicki, A. T.; Sivaram, S. V.; Jonker, B. T. A- and B-Exciton Photoluminescence Intensity Ratio as a Measure of Sample Quality for Transition Metal Dichalcogenide Monolayers. *APL Mater.* **2018**, *6*, 111106.
(53) Ma, C.; Yan, J.; Huang, Y.; Yang, G. Photoluminescence Manipulation of $WS_2$ Flakes by an Individual Si Nanoparticle. *Mater. Horiz.* **2019**, *6*, 97−106.
(54) Wei, K.; Liu, Q.; Tang, Y.; Ye, Y.; Xu, Z.; Jiang, T. Charged Biexciton Polaritons Sustaining Strong Nonlinearity in 2D Semiconductor-based Nanocavities. *Nat. Commun.* **2023**, *14*, 5310.
(55) Johnson, P. B.; Christy, R. W. Optical Constants of the Noble Metals. *Phys. Rev. B* **1972**, *6*, 4370−4379.
(56) Li, Y.; Chernikov, A.; Zhang, X.; Rigosi, A.; Hill, H. M.; van der Zande, A. M.; Chenet, D. A.; Shih, E.-M.; Hone, J.; Heinz, T. F. Measurement of the Optical Dielectric Function of Monolayer Transition-Metal Dichalcogenides: $MoS_2$, $MoSe_2$, $WS_2$, and $WSe_2$. *Phys. Rev. B* **2014**, *90*, 205422.
(57) Philipp, H. R. Optical Properties of Silicon Nitride. *J. Electrochem. Soc.* **1973**, *120*, 295.
(58) Malitson, I. H. Interspecimen Comparison of the Refractive Index of Fused Silica. *J. Opt. Soc. Am.* **1965**, *55*, 1205−1209.
(59) Wu, X.; Gray, S. K.; Pelton, M. Quantum-Dot-Induced Transparency in a Nanoscale Plasmonic Resonator. *Opt. Express* **2010**, *18*, 23633−23645.
(60) Niu, Y.; Xu, H.; Wei, H. Unified Scattering and Photoluminescence Spectra for Strong Plasmon-Exciton Coupling. *Phys. Rev. Lett.* **2022**, *128*, 167402.


https://doi.org/10.1021/acsanm.4c02981
*ACS Appl. Nano Mater.* XXXX, XXX, XXX−XXX